

Statistical analysis of circular-ribbon flares

YANJIE ZHANG,^{1,2} QINGMIN ZHANG,^{1,2} DECHAO SONG,^{1,2} SHUTING LI,^{1,2} JUN DAI,^{1,2} ZHE XU,³ AND HAISHENG JI^{1,2}

¹Key Laboratory of Dark Matter and Space Astronomy, Purple Mountain Observatory, CAS, Nanjing 210023, China

²School of Astronomy and Space Science, University of Science and Technology of China, Hefei 230026, China

³Yunnan Observatories, Chinese Academy of Sciences, 396 Yangfangwang, Guandu District, Kunming 650216, China

ABSTRACT

Circular-ribbon flares (CFs) are a special type of solar flares owing to their particular magnetic topology. In this paper, we conducted a comprehensive statistical analysis of 134 CFs from 2011 September to 2017 June, including four B-class, 82 C-class, 40 M-class, and eight X-class flares, respectively. The flares were observed by the Atmospheric Imaging Assembly (AIA) on board the Solar Dynamics Observatory (SDO) spacecraft. The physical properties of CFs are derived, including the location, area (A_{CF}), equivalent radius (r_{CF}) assuming a semi-spherical fan dome, lifetime (τ_{CF}), and peak SXR flux in 1–8 Å. It is found that all CFs are located in active regions, with the latitudes between -30° and 30° . The distributions of areas and lifetimes could be fitted with a log-normal function. There is a positive correlation between the lifetime and area. The peak SXR flux in 1–8 Å is well in accord with a power-law distribution with an index of -1.42 . For the 134 CFs, 57% of them are accompanied by remote brightenings or ribbons. A positive correlation exists between the total length (L_{RB}) and average distance (D_{RB}) of remote brightenings. About 47% and 51% of the 134 CFs are related to type III radio bursts and jets, respectively. The association rates are independent of flare energies. About 38% of CFs are related to mini-filament eruptions, and the association rates increase with flare classes. Only 28% of CFs are related to CMEs, meaning that a majority of them are confined rather than eruptive events. There is a positive correlation between the CME speed and peak SXR flux in 1–8 Å, and faster CMEs tend to be wider.

Keywords: Sun: flares — Sun: coronal mass ejections (CMEs) — Sun: filaments, prominences — Sun: UV radiation — Sun: radio radiation

1. INTRODUCTION

Since the first discovery in 1859 (Carrington 1859), solar flares have been observed and studied extensively (see Fletcher et al. 2011; Shibata & Magara 2011, and references therein). According to the classical two-dimensional (2D) flare model, i.e., the CSHKP model (Carmichael 1964; Sturrock 1966; Hirayama 1974; Kopp & Pneuman 1976), when high-energy electrons accelerated by magnetic reconnection propagate downward along the reconnected flare loops and hit the chromosphere, the localized plasmas at the footpoints are impulsively heated, forming two bright and elongated ribbons observed in ultraviolet (UV), extreme-ultraviolet (EUV), and $H\alpha$ wavelengths (Ji et al. 2006; Jing et al. 2016). In most cases, the ribbons separate due to continuing reconnection (Qiu et al. 2002). Aulanier et al. (2012) and Janvier et al. (2013) extended the 2D standard model to three dimensions to interpret the flare ribbons taking on double-J shapes.

Apart from the typical two-ribbon flares, there is another class of flares, i.e., circular-ribbon flares (CFs), whose ribbons are elliptical or circular (Masson et al. 2009). It

is generally believed that the three-dimensional (3D) magnetic configuration of CFs is composed of a null point and the associated dome-shaped fan-spine structure in the corona (e.g., Reid et al. 2012; Wang & Liu 2012; Jiang et al. 2013; Sun et al. 2013; Vemareddy & Wiegmann 2014; Joshi et al. 2015, 2021; Liu et al. 2015; Zhang et al. 2015, 2021; Mitra & Joshi 2021). Sometimes, the outer spine is embedded in a thin quasi-separatrix layer (QSL; Demoulin et al. 1996) where magnetic connectivity changes rapidly (Masson et al. 2009; Yang et al. 2015; Li et al. 2018). Magnetic reconnection preferentially occurs near the null point (Priest & Pontin 2009; Pontin et al. 2007, 2013; Yang et al. 2020b), and the closed ribbon is related to the intersection between the chromosphere and fan surface. Meanwhile, a shorter ribbon inside the closed ribbon is believed to be the intersection between the chromosphere and inner spine. The sizes of circular ribbons range from $\sim 30''$ (Wang & Liu 2012; Hao et al. 2017) to several $100''$ (Liu et al. 2013; Joshi et al. 2017; Hou et al. 2019; Chen et al. 2019; Lee et al. 2020a). The brightening of circular flare ribbons is not always simultaneous, but sequential in

some cases, which is probably caused by slip-running reconnection (Aulanier et al. 2007). The direction of brightening could be clockwise (Shen et al. 2019) or counterclockwise (Masson et al. 2009; Li et al. 2017, 2018; Xu et al. 2017). Interestingly, Zhang et al. (2020) reported fast degradation of a circular ribbon at speeds of 30–70 km s⁻¹ on 2014 August 24. Remote brightenings are frequently observed adjacent to the main flare site as a result of energy transport along the outer spine (Masson et al. 2009, 2017; Zhang et al. 2015; Hernandez-Perez et al. 2017; Li et al. 2017; Devi et al. 2020; Joshi et al. 2021). Extended remote brightenings with a length of ~400'' is investigated by Liu et al. (2020).

CFs are usually triggered by filament eruptions (Joshi et al. 2015; Xu et al. 2017; Song et al. 2018; Yang et al. 2020a), which may also generate coronal jets (Wang & Liu 2012; Joshi et al. 2018; Li & Yang 2019; Zhang et al. 2016a, 2021; Zhang & Ni 2019; Zhang 2020; Dai et al. 2021) or drive coronal mass ejections (CMEs; Sun et al. 2013; Joshi et al. 2015, 2017; Liu et al. 2019, 2020). CFs show similar dynamics to that of two-ribbon flares. Explosive chromospheric evaporation is detected in a C4.2 class flare by the Interface Region Imaging Spectrograph (IRIS; De Pontieu et al. 2014) on 2015 October 16 (Zhang et al. 2016a). The estimated energy flux of nonthermal electrons is adequate to account for the explosive evaporation. Imaging observation of converging hot ($\log T \approx 7.0$) plasma in a post flare loop is considered as direct evidence of chromospheric evaporation during the impulsive phase of a flare (Zhang et al. 2019a). Redshifts of a few 10 km s⁻¹ in the low-temperature emission lines (e.g., Si iv) are clear indications of chromospheric condensation at the circular flare ribbons (Zhang et al. 2016b, 2021). Besides, quasi-periodic pulsations (QPPs; Zimovets et al. 2021) produced by intermittent magnetic reconnections are identified in CFs (Kumar et al. 2015, 2016; Zhang et al. 2016b; Chen et al. 2019; Kashapova et al. 2020; Lee et al. 2020b; Li et al. 2020; Ning et al. 2022). The periods are between 20 s and 4 minutes in most cases. CFs are also accompanied by type III radio bursts (Zhang et al. 2016b, 2021) or type IV radio continuum emission (Chen et al. 2019). The total energies of CFs can reach up to 10³¹-10³³ erg. Zhang et al. (2019b) calculated various energy components in two successive M1.8 class CFs in NOAA active region (AR) 12434, including the peak thermal energy, nonthermal energy in flare-accelerated electrons, total radiative loss of the hot plasma, and radiative energy in 1–8 Å and 1–70 Å. It is revealed that the energy partitions in two flares are similar, and the heating requirement consisting of the peak thermal energy and radiative loss could sufficiently be supplied by the nonthermal energy. Further more, Cai et al. (2021) investigated four confined CFs in detail, finding that the values of energy components increase systematically with flare classes. The ratio

of nonthermal energy to magnetic free energy may provide a key factor for discriminating confined from eruptive flares.

So far, CFs have become a topic of great interest due to their particular configurations. However, statistical investigation of CFs is rare compared to two-ribbon flares (e.g., Crosby et al. 1993; Temmer et al. 2001; Veronig et al. 2002; Yashiro et al. 2006; Li et al. 2021; Lu et al. 2021) or microflares (Christe et al. 2008; Hannah et al. 2008). Song & Tian (2018) performed a statistical investigation of 90 CFs observed from 2010 June to 2017 December, finding that the occurrence rate of white-light (WL) flares increases with flare class. Moreover, the flares with WL enhancement have shorter durations, smaller sizes, stronger electric current, and more complicated magnetic field. Nevertheless, a comprehensive study of physical properties of CFs and related phenomena is scarce. In this paper, we carry out a statistical analysis of 134 CFs, including four B-class, 82 C-class, 40 M-class and eight X-class CFs (see Table 1). The paper is organized as follows. We describe the data analysis in Section 2. Statistical properties are presented in Section 3. Finally, a brief conclusion and discussions are given in Section 4.

2. DATA ANALYSIS

We searched for CFs observed by the Atmospheric Imaging Assembly (AIA; Lemen et al. 2012) on board the Solar Dynamics Observatory (SDO; Pesnell et al. 2012) from 2011 September to 2017 June. AIA took full-disk images in seven EUV (94, 131, 171, 193, 211, 304, and 335 Å) and two UV (1600 and 1700 Å) wavelengths. The AIA level_1 data with a time cadence of 12 s and a spatial resolution of 1''2 were calibrated using the standard program `aia_prep.pro` in the Solar Software (SSW). Photospheric line-of-sight (LOS) magnetograms of the flares were observed by the Helioseismic and Magnetic Imager (HMI; Scherrer et al. 2012) on board SDO. The HMI level_1 data with a time cadence of 45 s and a spatial resolution of 1''2 were calibrated using the standard program `hmi_prep.pro`. Soft X-ray (SXR) light curves of CFs in 1–8 Å were recorded by the GOES spacecraft. The associations with remote brightenings, coronal jets, and mini-filament eruptions were checked using the EUV observations of AIA. The total lengths of remote brightenings and average distances from the flare centers were calculated. The association with CMEs was examined using the WL observations from the Large Angle and Spectrometric Coronagraph (LASCO; Brueckner et al. 1995) on board the SOHO spacecraft. The LASCO/C2 has a field of view (FOV) of 2–6 R_⊙. Two databases were used: the CDAW catalog¹ where CMEs are identified manually and the CACTus website² where

¹ http://cdaw.gsfc.nasa.gov/CME_list

² <http://sidc.oma.be/cactus/scan>

CMEs are recognized automatically (Yashiro et al. 2008). The apparent linear velocities and angular widths of the associated CMEs were analyzed. The relation with type III radio bursts was checked using the radio dynamic spectra

recorded by the e-Callisto³ ground-based stations as well as the WAVES (Bougeret et al. 1995) instrument (0.02–13.825 MHz) on board the WIND spacecraft⁴.

Table 1. List of 134 Circular-ribbon Flares.

No.	NOAA AR	Date	GOES Class	Peak Flux (W m ⁻²)	Location	τ_{CF} (min)	A_{CF} (Mm ²)	L_{RB}/D_{RB} (Mm/Mm)	Jet	Type III	FE	V_{CME} (km s ⁻¹)	W_{CME} (°)
1	11283	2011 Sep 06	M5.3	5.39E-05	N15W09	94	2823.5	28.0/117.6	No	No	No	782	360
2	11283	2011 Sep 06	X2.1	2.16E-04	N15W20	35	2594.8	65.8/105.6	No	No	Yes	575	360
3	11283	2011 Sep 07	X1.8	1.80E-04	N16W32	81	1983.0	193.4/76.3	No	No	Yes	792	167
4	11283	2011 Sep 08	M6.7	6.77E-05	N16W42	64	2439.6	103.0/77.9	No	No	Yes	983	281
5	11324	2011 Oct 22	C4.1	4.12E-06	N11E24	34	1616.9	19.3/63.7	No	No	No	-	-
6	11339	2011 Nov 03	X1.9	2.04E-04	N21E64	102	725.8	65.2/35.7	No	No	Yes	991	360
7	11339	2011 Nov 06	M1.4	1.45E-05	N21E32	94	581.7	14.1/70.7	No	Yes	No	-	-
8	11339	2011 Nov 06	C8.8	9.10E-06	N21E30	43	542.6	35.7/67.5	No	No	No	-	-
9	11339	2011 Nov 06	C5.3	5.42E-06	N21E28	113	422.8	33.2/72.2	No	No	No	-	-
10	11346	2011 Nov 15	M1.9	1.97E-05	S19E32	99	1165.3	144.8/86.1	Yes	Yes	No	163	80
11	11346	2011 Nov 16	C2.8	2.91E-06	S18E19	31	315.8	91.3/75.2	Yes	No	Yes	-	-
12	11346	2011 Nov 16	C2.9	3.01E-06	S18E16	37	345.1	59.8/72.7	Yes	No	Yes	-	-
13	11346	2011 Nov 16	C5.0	5.14E-06	S19E12	59	1181.3	121.8/118.3	Yes	No	Yes	-	-
14	11346	2011 Nov 17	C2.0	2.05E-06	S19E04	59	1278.9	134.1/86.7	No	No	No	-	-
15	11476	2012 May 06	C1.4	1.43E-06	N11E72	12	354.0	-	No	No	No	-	-
16	11476	2012 May 07	C4.0	4.17E-06	N11E61	73	598.9	39.6/54.9	Yes	Yes	No	-	-
17	11476	2012 May 07	C7.9	8.07E-06	N13E60	24	428.0	78.3/67.7	No	Yes	No	-	-
18	11476	2012 May 07	C7.4	7.67E-06	N13E56	59	445.1	-	No	Yes	No	-	-
19	11476	2012 May 08	M1.4	1.48E-05	N13E45	92	545.6	60.1/92.3	No	Yes	Yes	-	-
20	11476	2012 May 09	M4.7	4.86E-05	N13E32	61	569.4	79.2/91.7	Yes	No	Yes	-	-
21	11476	2012 May 09	C1.5	1.55E-06	N13E28	11	424.1	-	Yes	No	No	-	-
22	11476	2012 May 09	M4.1	4.16E-05	N13E27	66	797.7	128.2/97.4	Yes	No	Yes	-	-
23	11476	2012 May 10	M5.7	6.00E-05	N13E23	101	1188.3	119.5/86.2	Yes	Yes	Yes	-	-
24	11476	2012 May 10	M1.7	1.84E-05	N13E14	83	979.8	82.5/98.5	Yes	No	Yes	-	-
25	11476	2012 May 11	C3.1	3.15E-06	N14E13	20	816.2	-	Yes	Yes	No	-	-
26	11476	2012 May 11	C3.5	3.69E-06	N14E06	11	485.9	-	Yes	Yes	No	-	-
27	11476	2012 May 14	C2.5	3.02E-06	N08W46	36	339.8	27.4/41.3	Yes	Yes	No	551	48
28	11598	2012 Oct 22	M5.0	5.10E-05	S13E64	113	1343.4	-	No	No	No	-	-
29	11598	2012 Oct 23	X1.8	1.71E-04	S13E59	108	1423.2	-	No	No	No	-	-
30	11652	2013 Jan 08	C1.8	1.92E-06	N21E56	25	343.5	-	Yes	No	No	-	-
31	11652	2013 Jan 12	C3.1	3.29E-06	N19W17	4	182.1	-	No	No	No	-	-
32	11652	2013 Jan 13	M1.0	1.25E-05	N18W18	16	311.1	-	Yes	Yes	No	-	-
33	11652	2013 Jan 13	C2.7	2.83E-06	N18W22	20	213.6	-	No	Yes	No	-	-
34	11652	2013 Jan 13	M1.7	1.86E-05	N18W22	9	362.1	56.2/115.2	Yes	Yes	Yes	696	46
35	11652	2013 Jan 14	C6.5	6.75E-06	N18W31	14	438.4	24.2/66.6	No	No	No	-	-
36	11669	2013 Feb 05	B6.6	6.92E-07	N09E64	63	1191.6	-	Yes	No	Yes	-	-
37	11669	2013 Feb 05	C6.3	6.51E-06	N08E62	25	1649.0	-	Yes	Yes	Yes	444	66
38	11675	2013 Feb 17	M1.9	2.80E-05	N12E21	10	183.0	7.0/47.7	Yes	Yes	No	-	-
39	11689	2013 Mar 12	C3.6	3.87E-06	S20W40	28	154.2	21.3/82.8	Yes	No	Yes	-	-

³ <http://www.e-callisto.org>

⁴ <https://solar-radio.gsfc.nasa.gov/wind/index.html>

Table 1. List of 134 Circular-ribbon Flares.

No.	NOAA AR	Date	GOES Class	Peak Flux (W m^{-2})	Location	τ_{CF} (min)	A_{CF} (Mm^2)	L_{RB}/D_{RB} (Mm/Mm)	Jet	Type III	FE	V_{CME} (km s^{-1})	W_{CME} ($^{\circ}$)
40	11731	2013 Apr 28	C3.7	4.07E-06	N09E28	9	335.2	-	Yes	Yes	No	-	-
41	11731	2013 Apr 28	C1.8	1.96E-06	N09E28	8	433.3	-	Yes	No	Yes	-	-
42	11731	2013 Apr 28	C3.6	4.02E-06	N09E27	13	133.2	-	Yes	Yes	No	-	-
43	11731	2013 Apr 29	C3.0	3.06E-06	N10E14	14	634.7	-	No	Yes	No	452	67
44	11731	2013 May 01	C1.1	1.14E-06	N07W11	10	160.8	-	Yes	No	Yes	-	-
45	11731	2013 May 02	M1.1	1.13E-05	N11W25	43	4539.9	-	Yes	Yes	Yes	-	-
46	11890	2013 Nov 05	M2.5	2.81E-05	S16E51	12	752.7	135.3/72.1	No	Yes	Yes	-	-
47	11890	2013 Nov 05	X3.3	3.85E-04	S13E45	23	796.4	61.8/79.4	Yes	Yes	Yes	562	195
48	11890	2013 Nov 06	C8.6	8.93E-06	S13E39	17	726.7	-	Yes	Yes	Yes	-	-
49	11890	2013 Nov 06	M3.8	3.88E-05	S13E36	21	701.0	169.8/149.8	No	Yes	Yes	347	122
50	11890	2013 Nov 07	M2.3	2.41E-05	S13E28	22	727.8	-	Yes	No	Yes	-	-
51	11890	2013 Nov 07	C5.9	5.99E-06	S13E23	21	697.8	-	No	Yes	Yes	-	-
52	11890	2013 Nov 08	X1.1	1.22E-04	S14E15	24	1485.7	311.1/120.9	Yes	Yes	Yes	-	-
53	11890	2013 Nov 10	X1.1	1.14E-04	S15W13	33	2171.1	381.0/119.1	Yes	Yes	Yes	682	262
54	11890	2013 Nov 10	C3.1	3.17E-06	S15W19	56	306.5	-	Yes	Yes	No	-	-
55	11890	2013 Nov 11	C6.4	6.59E-06	S15W26	33	521.0	39.6/110.1	No	No	Yes	-	-
56	11890	2013 Nov 11	C7.8	8.18E-06	S14W24	12	642.7	12.5/128.0	Yes	No	No	533	40
57	11890	2013 Nov 11	C5.0	5.09E-06	S14W34	25	1020.6	16.7/105.6	Yes	No	No	-	-
58	11890	2013 Nov 12	C3.1	3.22E-06	S11W60	12	346.8	-	Yes	No	No	365	24
59	11890	2013 Nov 13	C6.5	6.75E-06	S14W54	144	877.3	50.2/84.0	Yes	Yes	No	-	-
60	11936	2013 Dec 25	C1.7	1.79E-06	S18E51	58	621.2	-	No	No	No	254	72
61	11936	2013 Dec 27	C4.4	4.52E-06	S17E23	35	507.7	-	Yes	Yes	No	305	67
62	11936	2013 Dec 28	C3.0	3.08E-06	S17E09	38	931.1	32.3/49.2	No	Yes	Yes	-	-
63	11936	2013 Dec 28	C9.3	9.44E-06	S17E06	100	684.1	24.5/45.0	No	No	No	-	-
64	11936	2013 Dec 29	C3.1	3.17E-06	S17W01	9	451.6	-	No	Yes	No	-	-
65	11936	2013 Dec 29	M3.1	3.23E-05	S17W02	65	828.1	10.4/48.6	Yes	Yes	Yes	-	-
66	11936	2013 Dec 29	C5.1	5.26E-06	S16W06	60	831.7	7.7/48.9	No	No	No	-	-
67	11936	2013 Dec 29	C1.9	2.02E-06	S16W07	20	364.2	-	No	No	No	-	-
68	11936	2013 Dec 29	C5.4	5.57E-06	S16W09	61	647.6	218.6/103.0	Yes	No	No	-	-
69	11936	2013 Dec 31	M6.4	6.49E-05	S17W36	128	2582.3	240.5/88.9	No	Yes	Yes	-	-
70	11936	2014 Jan 01	M9.9	1.00E-04	S16W47	55	4240.8	116.8/84.2	No	No	Yes	326	113
71	11991	2014 Feb 27	C6.8	7.03E-06	S22E58	21	461.9	34.3/67.5	Yes	Yes	No	120	55
72	11991	2014 Feb 28	M1.1	1.22E-05	S23E52	61	333.6	123.5/59.6	Yes	No	No	-	-
73	11991	2014 Mar 05	C4.8	5.04E-06	S27W07	24	248.4	-	Yes	No	Yes	-	-
74	11991	2014 Mar 05	C2.8	2.90E-06	S27W08	79	248.9	-	Yes	No	No	-	-
75	11991	2014 Mar 05	M1.0	1.06E-05	S27W08	7	318.7	27.8/89.8	Yes	No	No	-	-
76	12017	2014 Mar 28	M2.0	2.06E-05	N12W21	42	2256.6	-	Yes	Yes	Yes	260	31
77	12017	2014 Mar 28	M2.6	2.67E-05	N12W24	37	2150.1	-	Yes	Yes	Yes	514	138
78	12017	2014 Mar 29	X1.0	1.02E-04	N11W33	64	2030.6	28.8/65.7	Yes	No	Yes	528	360
79	12031	2014 Apr 06	C3.8	3.96E-06	N03W23	66	1476.1	-	No	No	Yes	-	-
80	12035	2014 Apr 15	C8.6	9.08E-06	S15E25	21	1030.0	12.5/93.6	Yes	Yes	Yes	274	27
81	12035	2014 Apr 15	C7.3	7.92E-06	S14E21	47	2640.7	-	No	Yes	Yes	360	179
82	12035	2014 Apr 16	M1.0	1.04E-05	S13E08	33	1920.4	150.4/148.0	Yes	Yes	Yes	764	61
83	12036	2014 Apr 18	M7.3	7.32E-05	S17W29	138	23961.9	-	No	Yes	No	1203	360
84	12087	2014 Jun 13	M2.6	2.66E-05	S20E40	71	1004.1	33.0/91.5	Yes	Yes	No	370	42
85	12087	2014 Jun 13	C9.0	9.17E-06	S19E32	26	909.3	16.0/79.3	No	Yes	No	605	31
86	12127	2014 Jul 31	C1.3	1.44E-06	S07E32	8	193.0	-	Yes	Yes	Yes	458	77

Table 1. List of 134 Circular-ribbon Flares.

No.	NOAA AR	Date	GOES Class	Peak Flux (W m ⁻²)	Location	τ_{CF} (min)	A_{CF} (Mm ²)	L_{RB}/D_{RB} (Mm/Mm)	Jet	Type III	FE	V_{CME} (km s ⁻¹)	W_{CME} (°)
87	12146	2014 Aug 22	C2.2	2.22E-06	N11E01	88	3099.4	-	No	Yes	No	-	-
88	12148	2014 Aug 22	C6.6	6.71E-06	N08W32	27	394.4	7.2/87.4	Yes	No	No	-	-
89	12157	2014 Sep 13	C3.7	3.92E-06	S16W39	34	315.3	17.5/35.3	No	Yes	No	-	-
90	12192	2014 Oct 20	M1.4	1.57E-05	S15E46	21	508.6	-	Yes	Yes	No	-	-
91	12201	2014 Nov 03	C4.2	4.32E-06	S03E21	26	987.7	-	Yes	Yes	Yes	-	-
92	12227	2014 Dec 13	C4.0	4.10E-06	S03W66	36	1040.3	-	Yes	Yes	Yes	198	74
93	12242	2014 Dec 17	M8.7	8.76E-05	S22E09	162	13165.7	358.8/186.2	No	No	No	587	360
94	12266	2015 Jan 19	C3.3	3.41E-06	S06E04	23	415.0	-	Yes	No	Yes	-	-
95	12268	2015 Jan 29	C8.2	8.32E-06	S12W03	119	2071.2	26.9/129.6	No	No	No	-	-
96	12268	2015 Jan 29	M2.1	2.12E-05	S11W07	99	3042.0	30.9/116.0	No	Yes	No	-	-
97	12268	2015 Jan 29	C6.4	6.43E-06	S11W11	191	3235.1	31.2/112.5	No	No	No	-	-
98	12268	2015 Jan 30	M2.0	2.09E-05	S12W15	205	4132.4	37.3/104.7	No	No	No	-	-
99	12268	2015 Jan 30	M1.7	1.77E-05	S11W17	116	4783.7	87.8/87.2	No	No	No	-	-
100	12276	2015 Jan 30	C3.8	3.84E-06	S07E09	88	957.5	-	Yes	Yes	Yes	-	-
101	12277	2015 Feb 03	C3.9	3.98E-06	N07W04	43	599.0	14.2/77.4	Yes	Yes	Yes	-	-
102	12297	2015 Mar 09	C9.1	9.40E-06	S15E44	33	771.9	34.5/52.8	Yes	Yes	Yes	583	155
103	12297	2015 Mar 10	M5.1	5.29E-05	S14E39	25	1182.6	-	Yes	Yes	No	1040	360
104	12297	2015 Mar 10	C1.3	4.67E-06	S16E41	38	574.7	-	Yes	Yes	No	-	-
105	12297	2015 Mar 11	M2.9	2.97E-05	S15E27	85	591.8	-	No	Yes	No	702	160
106	12297	2015 Mar 12	M2.7	2.81E-05	S14E02	94	828.0	-	No	Yes	No	-	-
107	12297	2015 Mar 13	M1.8	1.89E-05	S14W03	80	710.5	-	Yes	Yes	No	-	-
108	12297	2015 Mar 15	C2.4	2.51E-06	S17W28	16	554.1	-	Yes	No	Yes	-	-
109	12297	2015 Mar 15	C1.0	1.04E-06	S17W40	21	346.6	-	Yes	No	No	-	-
110	12325	2015 Apr 16	C3.3	3.37E-06	N06E51	112	1177.4	12.8/47.5	No	No	No	-	-
111	12434	2015 Oct 15	C3.6	3.77E-06	S11E55	32	417.2	-	No	No	No	-	-
112	12434	2015 Oct 15	C3.9	4.07E-06	S11E53	34	627.7	-	No	No	No	-	-
113	12434	2015 Oct 15	C3.4	3.51E-06	S11E52	49	535.3	-	No	No	No	-	-
114	12434	2015 Oct 15	C3.1	3.22E-06	S12E51	47	440.8	29.5/92.2	No	No	No	283	13
115	12434	2015 Oct 15	M1.1	1.21E-05	S13E50	13	561.7	375.9/178.2	No	No	No	-	-
116	12434	2015 Oct 16	C3.4	3.58E-06	S13E45	16	569.5	95.7/167.6	Yes	Yes	No	-	-
117	12434	2015 Oct 16	C3.1	3.22E-06	S13E44	23	563.5	281.9/177.0	No	Yes	No	-	-
118	12434	2015 Oct 16	M1.1	1.14E-05	S13E46	26	599.0	282.8/177.8	No	Yes	Yes	-	-
119	12434	2015 Oct 16	C4.2	4.34E-06	S13E42	14	608.8	262.2/170.7	Yes	Yes	Yes	189	83
120	12434	2015 Oct 24	C1.3	1.35E-06	S13W73	29	720.4	-	Yes	No	No	-	-
121	12497	2016 Feb 13	C1.3	1.37E-06	N14W25	13	241.5	29.2/89.2	No	No	No	-	-
122	12497	2016 Feb 13	C2.8	2.85E-06	N14W26	27	281.5	25.1/83.1	Yes	No	No	278	19
123	12497	2016 Feb 13	B8.5	8.68E-07	N14W26	26	130.3	-	No	No	No	-	-
124	12497	2016 Feb 13	B6.9	7.03E-07	N14W27	51	123.1	-	No	No	No	-	-
125	12497	2016 Feb 13	M1.8	1.88E-05	N14W29	120	361.1	59.2/72.8	Yes	No	No	-	-
126	12497	2016 Feb 13	C1.6	1.67E-06	N14W31	26	400.8	49.0/66.4	No	No	No	-	-
127	12497	2016 Feb 14	C3.4	3.48E-06	N14W36	70	464.8	51.7/50.7	No	No	No	-	-
128	12497	2016 Feb 14	M1.0	1.05E-05	N14W48	39	987.2	52.7/85.5	No	No	No	-	-
129	12497	2016 Feb 15	C3.9	3.94E-06	N14W53	31	899.1	26.2/28.6	Yes	No	No	-	-
130	12567	2016 Jul 16	C6.8	7.11E-06	N05E26	35	260.6	19.4/31.4	No	No	No	-	-
131	12615	2016 Nov 30	C2.3	3.90E-06	S07E43	24	127.3	-	No	No	No	-	-
132	12661	2017 Jun 03	C2.1	2.16E-06	N07E56	77	636.9	-	No	Yes	Yes	-	-
133	12661	2017 Jun 03	C2.5	2.67E-06	N06E53	46	921.5	-	No	Yes	No	-	-

Table 1. List of 134 Circular-ribbon Flares.

No.	NOAA AR	Date	GOES Class	Peak Flux (W m^{-2})	Location	τ_{CF} (min)	A_{CF} (Mm^2)	L_{RB}/D_{RB} (Mm/Mm)	Jet	Type III	FE	V_{CME} (km s^{-1})	W_{CME} ($^{\circ}$)
134	12661	2017 Jun 05	B5.8	5.90E-07	N06E18	45	155.5	6.2/60.5	No	No	No	-	-

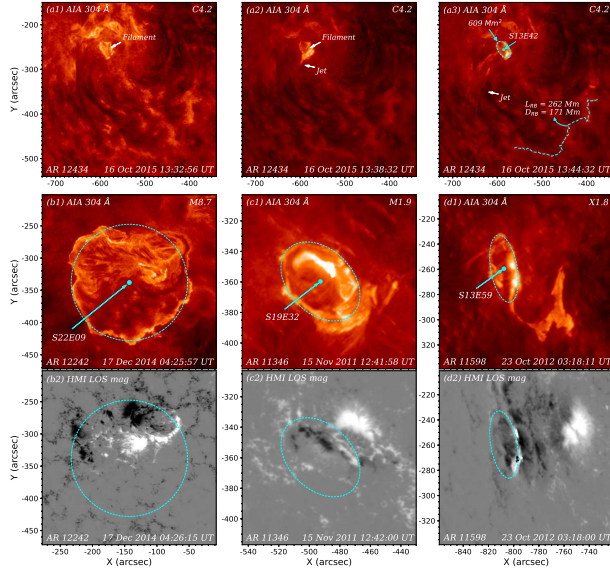


Figure 1. Top panels: Three snapshots of the AIA 304 Å images, showing the evolution of the C4.2 class flare in AR 12434 on 2015 October 16. The white arrows point to the accompanying mini-filament eruption and coronal jet. In panel (a3), the location and total area of the flare are labeled. The remote brightening is outlined by the cyan line. The total length and average distance between the flare and remote brightening are labeled. Middle panels: Additional three cases observed in 304 Å. The flare ribbons are fitted with a circle and two ellipses (dashed cyan lines). The centers are pointed by solid arrows. Bottom panels: Corresponding LOS magnetograms of the three events observed by HMI.

3. STATISTICAL PROPERTIES

3.1. Location

In Figure 1, the top panels show three images of the C4.2 class flare observed by AIA in 304 Å on 2015 October 16 (Zhang et al. 2016a; Dai et al. 2021). The flare was triggered by a mini-filament eruption and was associated with a blowout coronal jet. In panel (a3), the flare ribbon is fitted with an ellipse, whose center is considered as the flare location (S13E42). The middle panels of Figure 1 show 304 Å images of another three cases. The bright ribbons are fitted with a circle and two ellipses, which are drawn with dashed cyan lines. The centers (S22E09, S19E32, and S13E59) of the flares are derived and pointed by solid arrows. The bottom panels of Figure 1 show the corresponding LOS magnetograms of the three events observed by HMI. The CFs are characterized by a central positive (negative)

polarity surrounded by negative (positive) polarities, which is essentially consistent with the fan-spine magnetic structure (Masson et al. 2009; Wang & Liu 2012). Most of the CFs in our sample show similar characteristics. For all 134 events, we fit the circular or quasi-circular ribbons observed in 304 or 1600 Å with a circle or an ellipse. The derived coordinates of CFs in the sixth column of Table 1 agree with those recorded in the GOES flare catalog⁵. In Figure 2(a), the flare centers are marked with colored dots, with cyan (red) dots signifying confined (eruptive) flares, respectively. Figure 2(b) shows latitude distribution of the CFs, where 76 (58) of which are located in the southern (northern) hemisphere, respectively. It is clear that all CFs are located in ARs like microflares, and the latitudes of CFs are between -30° and 30° . Hence, the distribution of CFs is consistent with the AR belts.

3.2. Area

Compared with two-ribbon flares whose ribbons show separation (Qiu et al. 2002) or elongation (Li et al. 2015; Qiu et al. 2017), the outer ribbons of CFs hardly expand. Hence, the area keeps constant. In Figure 1(a3), the apparent area of the C4.2 flare enclosed by the ellipse is $\sim 452 \text{ Mm}^2$. The true area ($\sim 609 \text{ Mm}^2$) after deprojection according to the flare longitude is defined as the total area (A_{CF}). In the middle panels of Figure 1, the apparent areas of the three CFs are ~ 13008 , ~ 985 and $\sim 739 \text{ Mm}^2$. The true areas are estimated to be ~ 13166 , ~ 1165 and $\sim 1423 \text{ Mm}^2$, respectively. For the 134 CFs, the areas are calculated according to the fitted circles or ellipses, which range from 123 to $\sim 5000 \text{ Mm}^2$ in most cases. Figure 3 shows the distribution of A_{CF} . Note that the areas (13166 and 23962 Mm^2) of two events significantly exceeding 5000 Mm^2 are not taken into account in the histogram. We fit the distribution of A_{CF} with a log-normal function (Zhang et al. 2010):

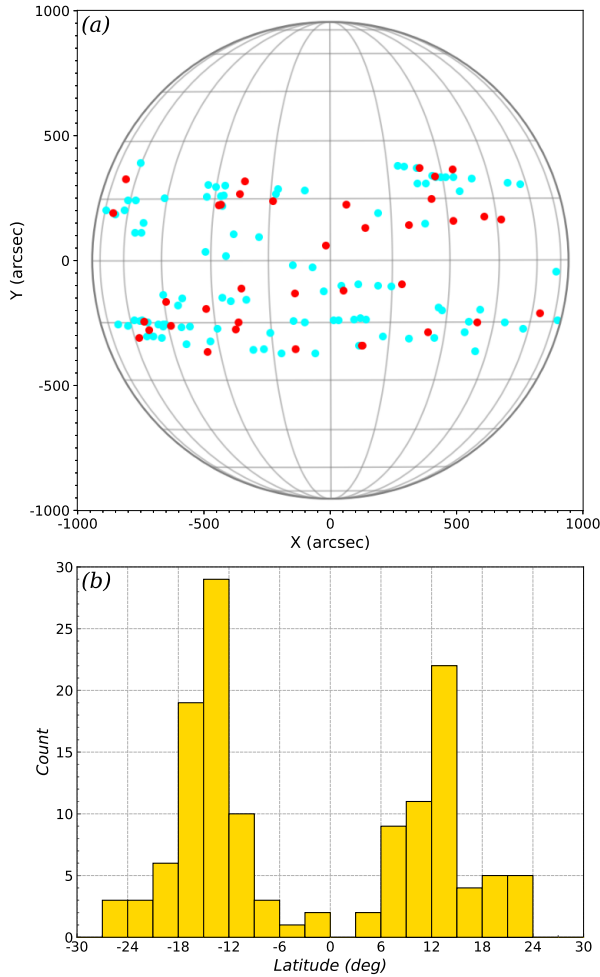
$$\frac{1}{N} \frac{dN}{dx} = f(x, \mu, \sigma) = \frac{1}{x\sigma\sqrt{2\pi}} e^{-\frac{(\ln x - \mu)^2}{2\sigma^2}}, x > 0. \quad (1)$$

The curve fitting is performed by using `mpfit.pro` and the result is superposed with a red line in Figure 3, where $\mu = 6.51$ and $\sigma = 0.66$.

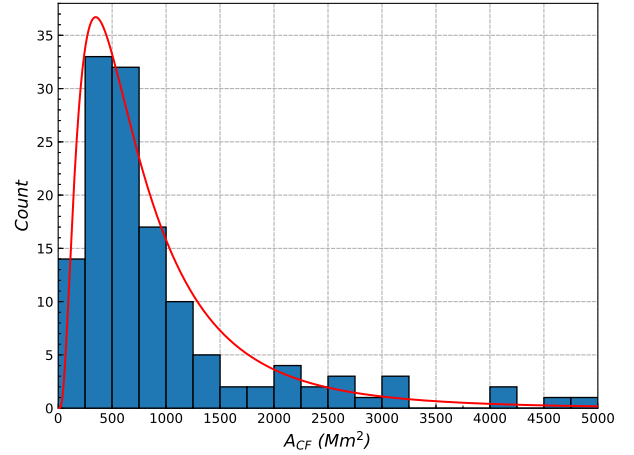
⁵ https://hesperia.gsfc.nasa.gov/goes/goes_event_listings/

Table 2. Minima, maxima, mean values, and median values of the physical properties of CFs and the related activities.

parameter	A_{CF}	r_{CF}	τ_{CF}	L_{RB}	D_{RB}	V_{CME}	W_{CME}
	(Mm ²)	(Mm)	(minute)	(Mm)	(Mm)	(km s ⁻¹)	(°)
Minimum	123.1	6.3	4.0	6.2	28.6	120.0	13.0
Maximum	23961.9	87.3	205.0	381.0	186.2	1203.0	360.0
Mean	1214.8	16.8	49.6	84.1	89.1	516.7	143.6
Median	631.2	14.2	35.0	44.3	84.8	514.0	80.0


Figure 2. (a) Locations of the 134 CFs, which are marked with cyan dots (confined flares) and red dots (eruptive flares), respectively. The latitudes and longitudes of the Sun are drawn with gray lines. (b) Latitude distribution of the CFs. Positive (negative) latitude means northern (southern) hemisphere, respectively.

We notice that there is a tendency of increasing area with flare class. In Figure 4(a), the flare areas are divided into three groups of roughly the same amount. In the range of 0–462 Mm², only 13% (6/45) are M- and X-class CFs. The


Figure 3. Distribution of the flare area. The result of curve-fitting using the log-normal function is superposed with a red line. Two values significantly exceeding 5000 Mm² are excluded in this plot.

proportion rises to 36% (16/45) in the range of 462–915 Mm². Above 915 Mm², M- and X-class CFs account for 59% (26/44). Therefore, flares with larger magnitudes generally have larger areas. The sample of CFs in our study overlaps with that in Song & Tian (2018). They used an irregularly closed line rather than a circle or an oval to fit the flare ribbon. Although the methods are different, the derived areas of CFs are very close to each other.

It is widely believed that the magnetic configuration of CFs consist of a null point and the associated dome-shaped fan-spine structure. Assuming that the fan surface is semi-sphere (Pariat et al. 2009, 2010), the height of null point is equivalent to the radius of circular ribbons:

$$h_{NP} = r_{CF} = \sqrt{\frac{A_{CF}}{\pi}}. \quad (2)$$

Figure 5 shows the distribution of r_{CF} , which lies in the range of 6–39 Mm with a mean value of ~ 16 Mm (the largest two events are excluded). The estimated altitudes of null points are consistent with previous results (e.g., Sun et al. 2013; Xu et al. 2017; Hou et al. 2019; Li & Yang 2019; Yang et al. 2020b). Song & Tian (2018) found that

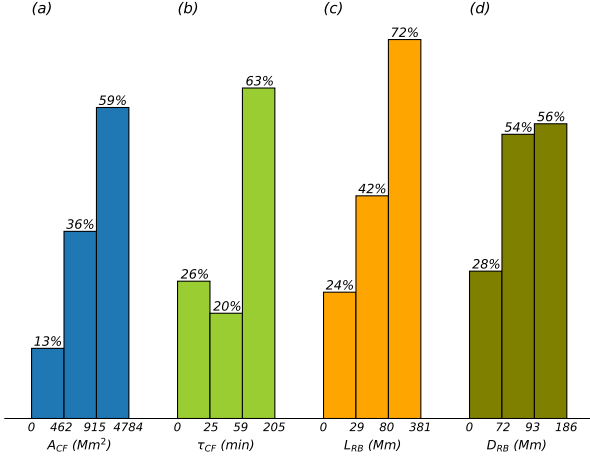


Figure 4. Percentages of M- and X-class CFs in different groups of area (a), lifetime (b), total length of remote brightening (c), and average distance of remote brightening (d).

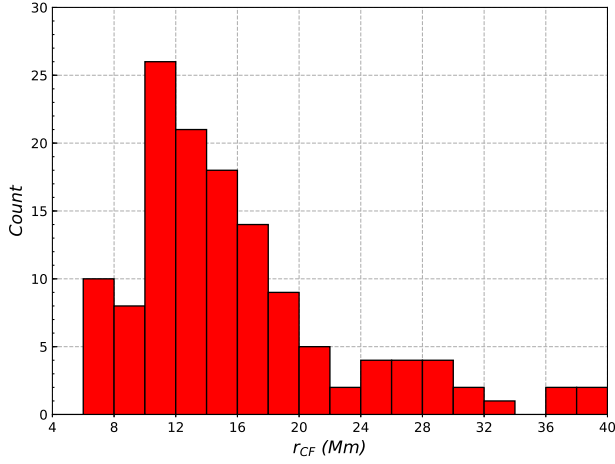


Figure 5. Distribution of the equivalent radius of flare ribbons.

WL flares feature smaller areas than normal flares with the same flare magnitude, which is explained by the lower heights of null points where magnetic free energy is released and consequently larger energy fluxes in WL flares.

3.3. Lifetime

We determine the flare lifetime (τ_{CF}) using the start and end times. The former refers to the time when the GOES 1–8 Å flux begins to increase rapidly, and the latter refers to the time when the flux declines to a nearly constant level. In Figure 6, the bottom panels show AIA 131 Å images of the M8.7 class flare occurring in AR 12242 on 2014 December 17 (Chen et al. 2019). The top panel shows the SXR light curve of the flare. The black dashed lines denote the start time (04:25:34 UT), peak time (04:51:34 UT), and end time (07:07:34 UT) of the flare. The lifetime reaches ~162 minutes accordingly.

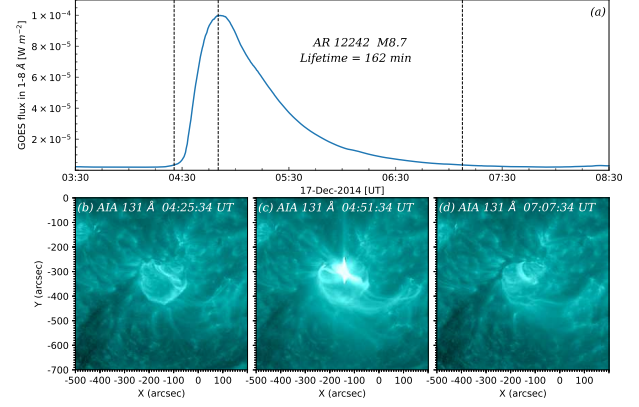


Figure 6. (a) SXR light curve of the M8.7 class flare occurring in AR 12242 on 2014 December 17. The three black dashed lines denote the start, peak, and end times of the flare. (b–d) AIA 131 Å images of the flare.

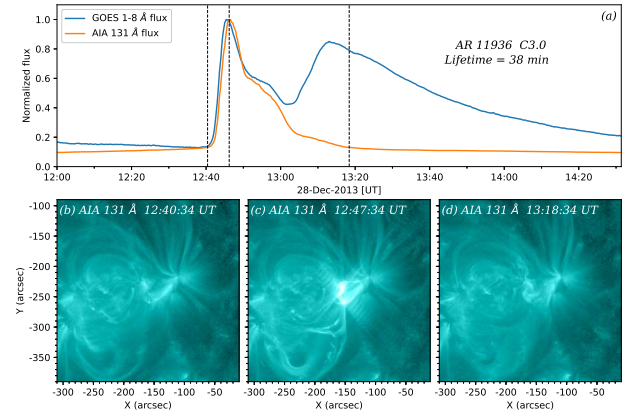


Figure 7. (a) SXR light curve (blue line) and 131 Å light curve (orange line) of the C3.0 class flare occurring in AR 11936 on 2013 December 28. The three black dashed lines denote the start time (12:40:34 UT), first peak time (12:47:34 UT), and end time (13:18:34 UT). There is only one peak in the EUV light curve, which corresponds to the first peak in SXR. The second peak (~13:14:55 UT) in SXR is unrelated to the C3.0 class flare. Hence, the lifetime of flare is ~38 minutes, which is considerably shorter than the M8.7 flare.

If the SXR light curve has a second peak in the decay phase, which is probably due to another eruption somewhere else, the AIA 131 Å light curve of the relevant flare is used as a supplementary to determine τ_{CF} . In Figure 7, the bottom panels show AIA 131 Å images of the C3.0 class flare occurring in AR 11936 on 2013 December 28. The top panel shows the SXR light curve (blue line) and 131 Å light curve (orange line) of the flare, respectively. The black dashed lines denote the start time (12:40:34 UT), first peak time (12:47:34 UT), and end time (13:18:34 UT). There is only one peak in the EUV light curve, which corresponds to the first peak in SXR. The second peak (~13:14:55 UT) in SXR is unrelated to the C3.0 class flare. Hence, the lifetime of flare is ~38 minutes, which is considerably shorter than the M8.7 flare.

Figure 8 shows the distribution of τ_{CF} with a mean value of ~50 minutes, which is two times larger than that of Ly α flares (Lu et al. 2021). Likewise, the distribution can be fit-

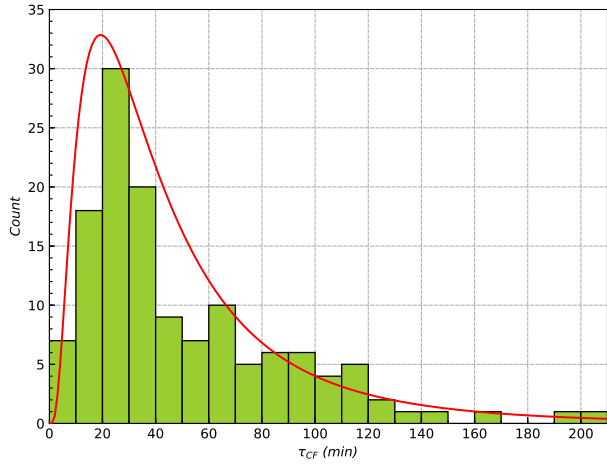


Figure 8. Distribution of the lifetime of CFs. The result of curve-fitting using the log-normal function is superposed with a red line.

ted with a log-normal function in Equation 1. The fitted curve is superposed with a red line, where $\mu = 3.60$ and $\sigma = 0.64$. To explore the relationship between area and lifetime of CFs, we draw a scatter plot in Figure 9. The two parameters have a positive correlation with a coefficient of ~ 0.5 . The timescale of conductive cooling of hot flare loops is expressed as (Cargill 1994; Zhang et al. 2019a):

$$\tau_{cc} = 4 \times 10^{-10} \frac{n_e L^2}{T_e^{5/2}}, \quad (3)$$

where n_e , T_e , and L represent the electron number density, temperature, and total length of a flare loop. For CFs with fan-spine topology, $A_{CF} \propto L^2 \propto \tau_{cc}$. That is to say, for flares with larger sizes, the cooling times become longer, which can easily interpret the linear correlation between A_{CF} and τ_{CF} .

According to the lifetime, we divide the 134 flares into three groups of the same amount, i.e., 0–25, 25–59, and 59–205 minutes. The percentages of M- and X-class CFs in the three groups are 26% (12/46), 20% (9/45), and 63% (27/43) (see Figure 4(b)). Hence, flares with larger magnitudes tend to have longer lifetimes. In the statistical investigation of CFs (Song & Tian 2018), the end time corresponds to the time when the flux decreases to a point halfway between the peak flux and the pre-flare level, leading to an average lifetime of 10–20 minutes, which is systematically shorter than our results. Besides, some of the CFs may experience an EUV late phase after the main flare phase observed in “warm” emission lines (e.g., 335 Å) as a result of additional heating (Sun et al. 2013). The much extended lifetimes in EUV 335 Å compared with SXR lifetimes are out of the scope of this study.

3.4. Peak SXR flux in 1–8 Å

For the 134 CFs, the peak SXR flux in 1–8 Å ranges from $\sim 5.9 \times 10^{-7}$ to $\sim 3.9 \times 10^{-4} \text{ W m}^{-2}$. Figure 10 shows the distri-

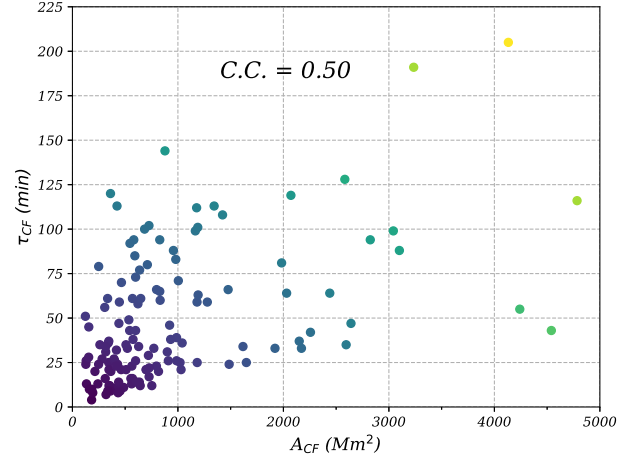


Figure 9. Scatter plot between the area (A_{CF}) and lifetime (τ_{CF}) of CFs. The correlation coefficient is ~ 0.50 .

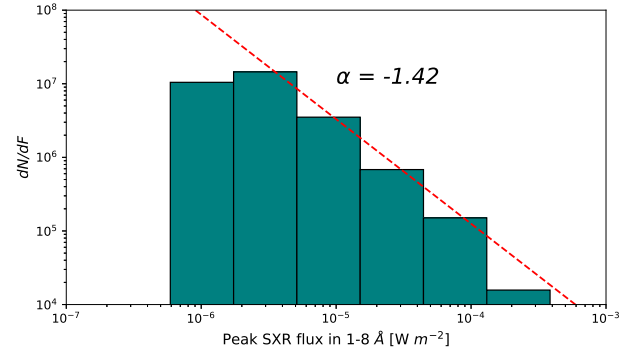


Figure 10. Distribution of the peak SXR flux in 1–8 Å. The power-law index α is labeled.

bution of the peak SXR flux. It is clear that the distribution could be nicely fitted with a power-law function (e.g., Dennis 1985; Lu & Hamilton 1991; Crosby et al. 1993; Christe et al. 2008) above $\sim 2 \times 10^{-6} \text{ W m}^{-2}$:

$$\frac{dN}{dF} \propto F^\alpha, \quad (4)$$

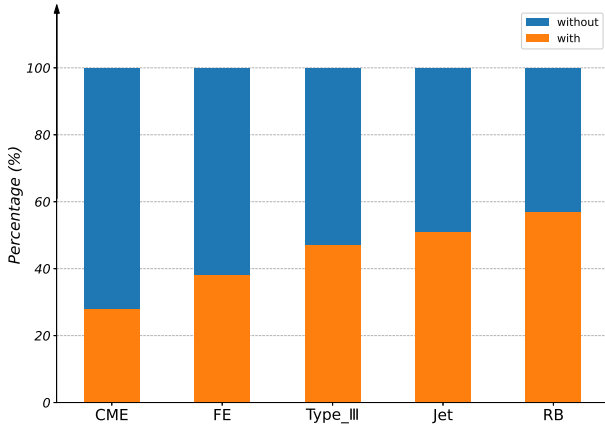
where F denotes the peak flux, and $\alpha = -1.42$ denotes the power-law index. The value of α is close to that of microflares at 3–6 keV and less than that of Ly α flares (Lu et al. 2021).

3.5. Relation with remote brightenings

As mentioned in Section 1, CFs are usually associated with remote brightenings or remote ribbons (Masson et al. 2009; Xu et al. 2017; Song et al. 2018; Chen et al. 2019). In Figure 1(a3), remote brightenings appear to the southwest of the C4.2 class flare, which is overlaid with a cyan line. The brightening has a total length (L_{RB}) of $\sim 262 \text{ Mm}$ and an average distance (D_{RB}) of $\sim 171 \text{ Mm}$ away from the flare center.

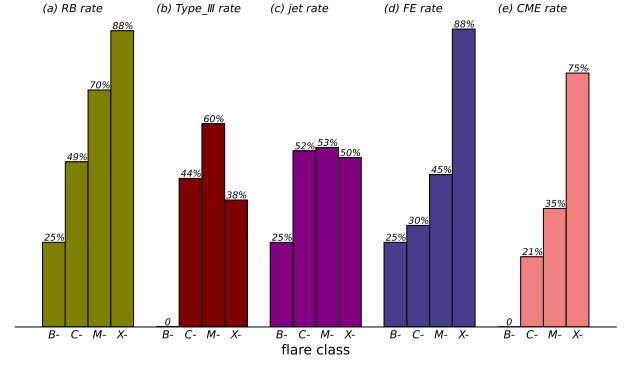
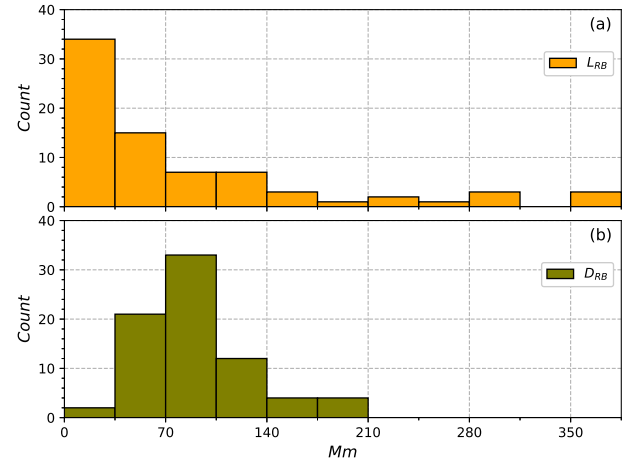
Table 3. Numbers of CFs associated with RBs, type III radio bursts, jets, mini-filament eruptions, and CMEs.

activity	B-class	C-class	M-class	X-class	total
CF	4	82	40	8	134
RB	1	40	28	7	76
type III	0	36	24	3	63
jet	1	43	21	4	69
FE	1	25	18	7	51
CME	0	17	14	6	37

**Figure 11.** Proportions of CFs related to remote brightenings, type III radio bursts, jets, mini-filament eruptions (FEs), and CMEs.

For the 134 CFs in this study, we searched for remote brightenings observed by AIA mainly in 304 and 1600 Å, finding that $\sim 57\%$ (76/134) of CFs have associated remote brightenings, which is shown in Figure 11. Specifically, the association rates with B-, C-, M-, and X-class flares are 25%, 49%, 70%, 88%, respectively (see Figure 12(a) and Table 3). The increasing rate with flare magnitude indicates that larger flares are more likely to produce remote brightenings. The total length of remote brightening or ribbon is denoted with L_{RB} , and the average distance from the flare center is denoted with D_{RB} . Figure 13 shows the distributions of L_{RB} and D_{RB} . It is revealed that L_{RB} lies in the range of 6.2–381.0 Mm, with a mean value of ~ 84.1 Mm. D_{RB} lies in the range of 28.6–186.2 Mm, with a mean value of ~ 89.1 Mm. Figure 14 shows the scatter plot between L_{RB} and D_{RB} , indicating a good correlation between the two parameters with a correlation coefficient of ~ 0.65 . In other words, remote brightenings further away from the main CFs are more likely to have longer extensions. A linear fitting (red dashed line) between the two parameters is performed, i.e.,

$$D_{RB} = 67.56 + 0.26L_{RB}. \quad (5)$$

**Figure 12.** Association rates of CFs with remote brightenings (a), type III radio bursts (b), jets (c), mini-filament eruptions (d), and CMEs (e) for B-, C-, M-, and X-class flares, respectively.**Figure 13.** Distributions of the total length (L_{RB}) and average distance (D_{RB}) of remote brightenings associated with CFs.

To investigate the relationship between flare magnitude and association with remote brightenings, we divide L_{RB} and D_{RB} into three groups with the same numbers. The values of L_{RB} are divided into 0–29, 29–80, and 80–381 Mm. The values of D_{RB} are divided into 0–72, 72–93, and 93–186 Mm. The percentages of M- and X-class CFs in each group are plotted in Figure 4(c-d). The percentages increase systematically with both parameters, indicating that flares with larger magnitudes are more likely to produce longer remote brightenings or ribbons. In the 3D numerical simulations of jets confined by large-scale coronal loops (Wyper & DeVore 2016; Wyper et al. 2016), the aspect ratio of the fan-spine structure is between 1.0 and 2.7. In our study, the aspect ratio is defined as $\frac{D_{RB}}{2r_{CF}}$, which has a range of 0.8–6.7 and a mean value of ~ 2.9 . Hence, the results will impose constraints on numerical simulations of CFs in the future (Pontin et al. 2013).

3.6. Relation with type III radio bursts

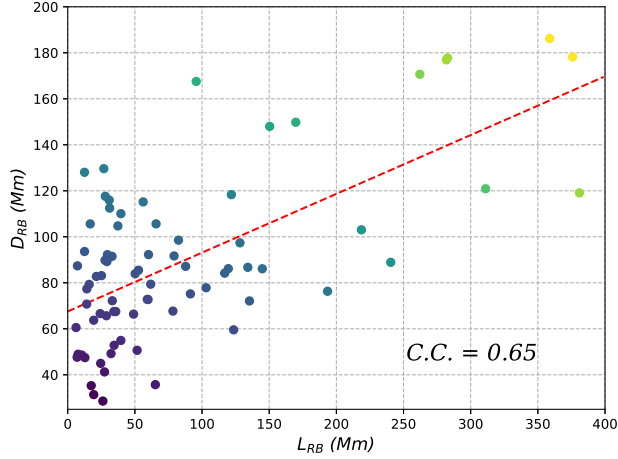


Figure 14. Scatter plot between the total length (L_{RB}) and average distance (D_{RB}) of remote brightenings. The result of linear fitting is plotted with a red dashed line. The correlation coefficient (~ 0.65) is labeled.

Flare-accelerated nonthermal electrons propagating along open field lines are capable of producing type III radio bursts (Benz et al. 2005; Morosan et al. 2014; Reid & Ratcliffe 2014; Zhang et al. 2015). In Figure 15, the top panel shows the 304 Å image of an M1.4 class CF in AR 11476 on 2012 May 8. The corresponding radio dynamic spectra recorded by the e-Callisto/BLEN7M station is displayed in the bottom panel. It is obvious that type III radio bursts around 700 MHz with fast frequency drift occur during the impulsive phase, when the release rate of magnetic free energy is maximum. The existence of radio bursts is confirmed by the WIND/WAVES observation.

For the 134 CFs, 47% (63/134) of them are accompanied with type III bursts during the impulsive phases, which is displayed in Figure 11. Note that those occurring in the pre-flare or decay phases are considered as unrelated events, which may result in an underestimate of the total amount. In Figure 12(b), the proportions of CFs related to type III bursts at various flare magnitudes are demonstrated, being 0%, 44%, 60%, and 38% for B-, C-, M-, and X-class CFs, respectively. The relatively lower proportion in B-class flares may be due to the limited number of sample. Hence, there is no correlation between the flare magnitude and type III bursts. In other words, the production of type III bursts depends mainly on the magnetic topology instead of flare energy (Krucker et al. 2011; Glesener et al. 2012; Duan et al. 2022).

3.7. Relation with coronal jets

As mentioned in Section 1, CFs are frequently associated with hot coronal jets observed in EUV wavelengths (Li & Yang 2019; Zhang & Ni 2019; Zhang 2020; Zhang et al. 2021) or cool surges observed in H α (Wang & Liu 2012; Xu et al. 2017). In Figure 1, the C4.2 class flare is accompanied by a blowout jet (Zhang et al.

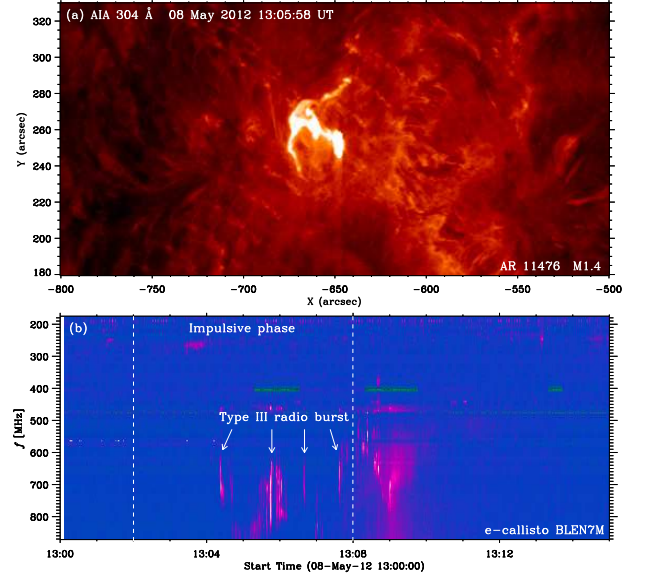


Figure 15. (a) AIA 304 Å image of the M1.4 class CF occurring in AR 11476 on 2012 May 8. (b) Radio dynamic spectra of the flare recorded by the e-Callisto/BLEN7M station. The arrows point to the type III radio bursts. The white dashed lines mark the start and peak times of the flare.

2016a; Dai et al. 2021). For the 134 events, about half of them are accompanied by jets in 304 Å, which is displayed in Figure 11. In Figure 12(c), the proportions of CFs related to jets at various flare magnitudes are demonstrated, being 25%, 52%, 53%, and 50% for B-, C-, M-, and X-class flares, respectively. Therefore, there is no preference of jet production for CFs with larger magnitudes as well (Chae et al. 1999; Shibata et al. 2007; Duan et al. 2022).

3.8. Relation with mini-filament eruptions

The occurrence of CFs is often associated with filament or minifilament eruptions (Wang & Liu 2012; Jiang et al. 2013; Sun et al. 2013; Yang & Zhang 2018). In this scenario, breakout-type magnetic reconnection takes place near the null point after the filament embedded in the fan dome rises up (Joshi et al. 2015; Wyper et al. 2017). The initiation of filament eruption may result from magnetic flux emergence (Li et al. 2017), rotation (Xu et al. 2017), or ideal MHD instabilities. The null-point reconnection not only accelerates nonthermal electrons to produce the circular ribbon in the chromosphere, but speeds up the filament eruption as well (Zhang et al. 2021).

Most of the homologous CFs in AR 12434 are triggered by mini-filament eruptions (Zhang et al. 2016a, 2021). Figure 1(a2) shows the AIA 304 Å image of the C4.2 class flare, and the mini-filament within the circular ribbon is pointed by the arrow. For the 134 events, 38% (51/134) of them are associated with filament eruptions, which is displayed in Figure 11. Figure 12(d) shows the proportions of CFs related

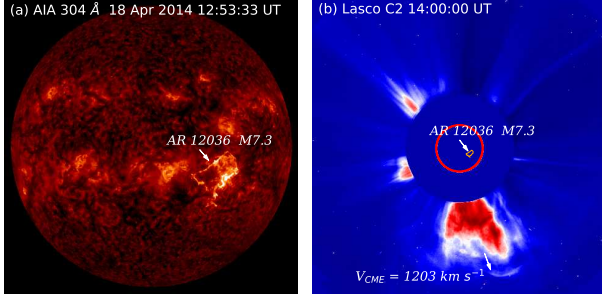


Figure 16. (a) AIA 304 Å image of the M7.3 class flare in AR 12036 on 2014 April 18. (b) WL image of the associated CME at a speed of 1203 km s⁻¹ in the LASCO/C2 FOV.

to mini-filament eruptions: 25% (1/4), 30% (25/82), 45% (18/40) and 88% (7/8) for B-, C-, M-, and X-class flares, respectively. The increasing proportions with flare classes indicate that larger flares are more likely to be triggered by filament eruptions.

3.9. Relation with CMEs

As mentioned in the previous section, CFs are sometimes triggered by filament or minifilament eruptions. The eruption may also drive a CME observed in the WL coronagraphs (Joshi et al. 2017; Liu et al. 2020; Kumar et al. 2021). In Figure 16, the left panel shows the 304 Å image of the M7.3 class CF in AR 12036 on 2014 April 18 (Joshi et al. 2015). The associated CME at a speed of ~ 1203 km s⁻¹ in the LASCO/C2 FOV is displayed in the right panel. For the 134 CFs, only 28% (37/134) of them are related to CMEs, which is shown in Figure 11. It is evident that the association rate with CMEs is the lowest while the association rate with remote brightenings is the highest in our investigation. In other words, most of ($\sim 72\%$) CFs are confined rather than eruptive (Wyper & DeVore 2016; Li et al. 2018; Yang & Zhang 2018). The CME association rates for B-, C-, M-, X-class flares are 0%, 21%, 35%, and 75%, which is displayed in Figure 12(e). The increasing CME rates with flare magnitudes are consistent with previous findings, suggesting that larger flares are more likely to produce CMEs (Yashiro et al. 2005, 2006). The low percentage of CMEs is expected, since magnetic flux ropes are required to generate CMEs in most cases (Vourlidas et al. 2013). For eruptive flares, two parallel ribbons or S-shaped ribbons appear on both sides of the polarity inversion lines (Aulanier et al. 2012; Janvier et al. 2013; Savcheva et al. 2016). Therefore, the formation of a CF is unlikely in this situation.

The distribution of the linear speed (V_{CME}) of the 37 CMEs is drawn in Figure 17. The values of V_{CME} lie in the range of 120–1203 km s⁻¹, with an average speed of ~ 517 km s⁻¹, which is slightly higher than that of CMEs near solar maximum (Yashiro et al. 2004). Figure 18 shows the scatter plot between the peak flux in 1–8 Å and V_{CME} of the 37 eruptive

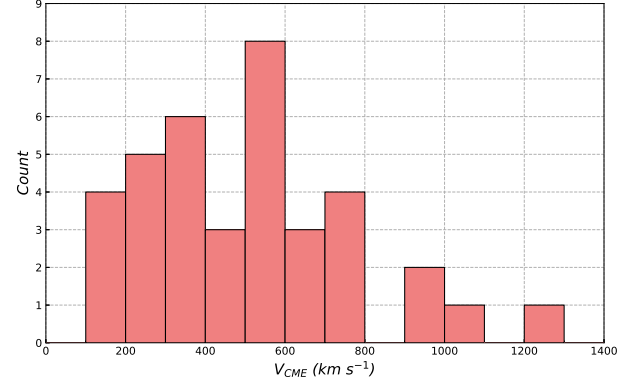


Figure 17. Distribution of the CME speed (V_{CME}) related to CFs.

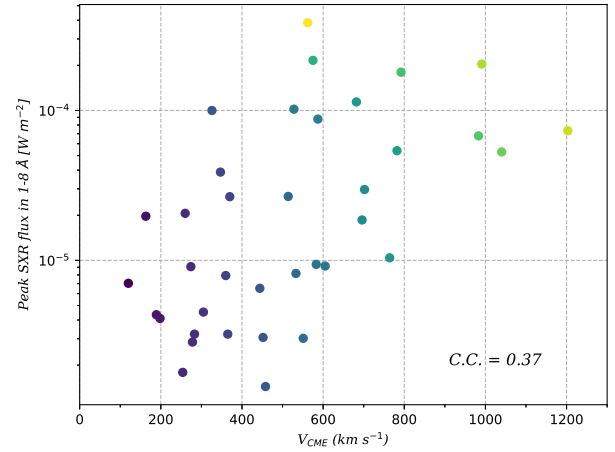


Figure 18. Scatter plot between the peak SXR flux in 1–8 Å of CFs related to CMEs and V_{CME} . The correlation coefficient is ~ 0.37 .

flares. A positive correlation is clearly demonstrated with a correlation coefficient of ~ 0.37 , which is consistent with previous finding that CMEs associated with X-class flares are remarkably faster than those of CMEs associated with C-class flares (Yashiro et al. 2005).

Out of the 37 CMEs, 30 of them are normal or partial halo CMEs, and seven of them are full halo CMEs. Some of them are jet-like, narrow CMEs with angular width (W_{CME}) less than 25°. Figure 19 and Figure 20 show scatter plots between W_{CME} and peak flux of flare and V_{CME} , respectively. It is clear that W_{CME} have positive correlations with flare peak flux and V_{CME} . Note that full halo CMEs ($W_{CME} = 360^\circ$) are not included when calculating the correlation coefficients. The result in Figure 20 suggests that faster CMEs tend to be wider, which is in line with previous statistical investigation (Yashiro et al. 2004).

According to their speeds, the 37 CMEs are divided into three groups with roughly the same numbers. Figure 21(a) shows that the percentages of M- and X-class CFs are 33% (4/12), 42% (5/12) and 85% (11/13) for 0–360, 360–583, and 583–1203 km s⁻¹, respectively. The association rates of

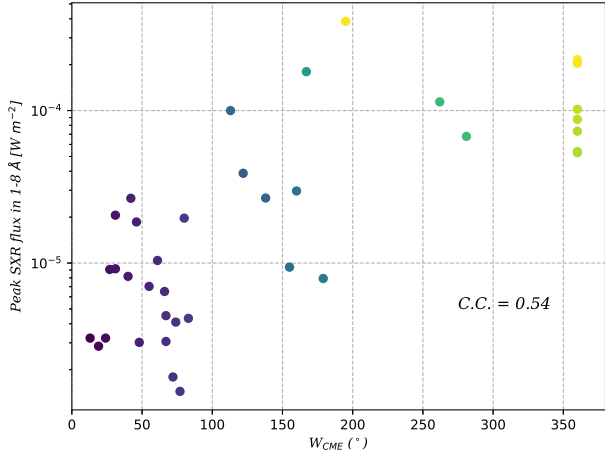


Figure 19. Scatter plot between the peak SXR flux in 1-8 Å of CFs related to CMEs and the CME angular widths (W_{CME}). The correlation coefficient is ~ 0.54 .

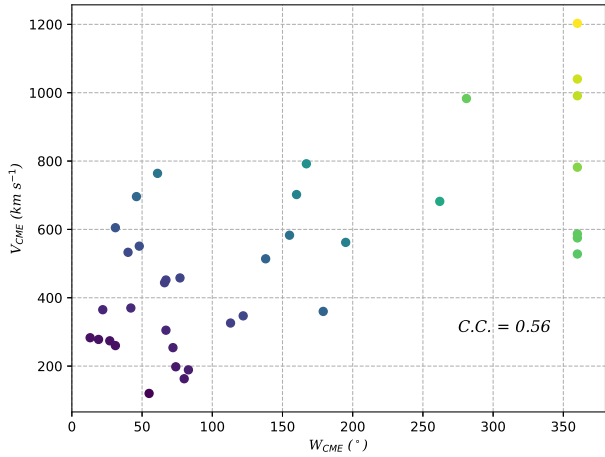


Figure 20. Scatter plot between V_{CME} and W_{CME} , indicating faster CMEs tend to be wider. The correlation coefficient is ~ 0.56 .

CMEs with big flares increase with the CME speeds, which is consistent with the fact that faster CMEs are more related to flares with larger magnitudes (Yashiro et al. 2005, 2006). Figure 21(b) shows the percentages of filament eruptions for the three groups of CMEs, being 50% (6/12), 58% (7/12) and 54% (7/13). The association rates of CMEs with filament eruptions are independent of the CME speeds.

Fast CMEs are capable of driving shock waves, which are associated with type II radio bursts (e.g., Ontiveros & Vourlidis 2009; Zucca et al. 2018; Mancuso et al. 2019). For the 37 eruptive CFs accompanied by CMEs, seven of which are associated with type II bursts, including two X-class (No. 3, 53) and five M-class (No. 34, 49, 77, 82, 83) flares. In Figure 22, the left panels show three CFs observed in 131 Å. The middle panels show the corresponding CMEs observed by LASCO/C2, with the apparent speeds being labeled. The related shock waves with

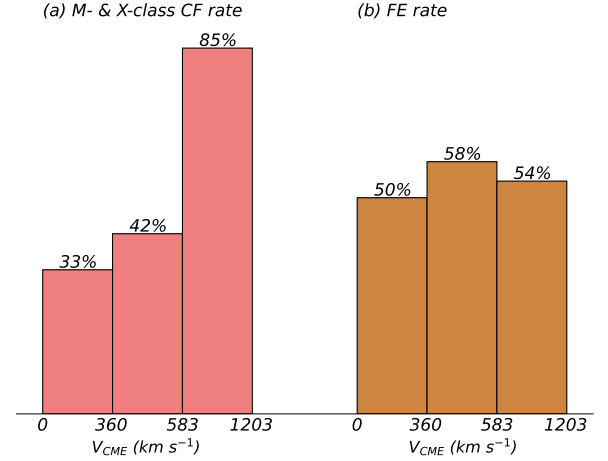


Figure 21. (a) Percentages of M- and X-class flares for the three groups of CMEs. (b) Percentages of mini-filament eruptions for the three groups of CMEs.

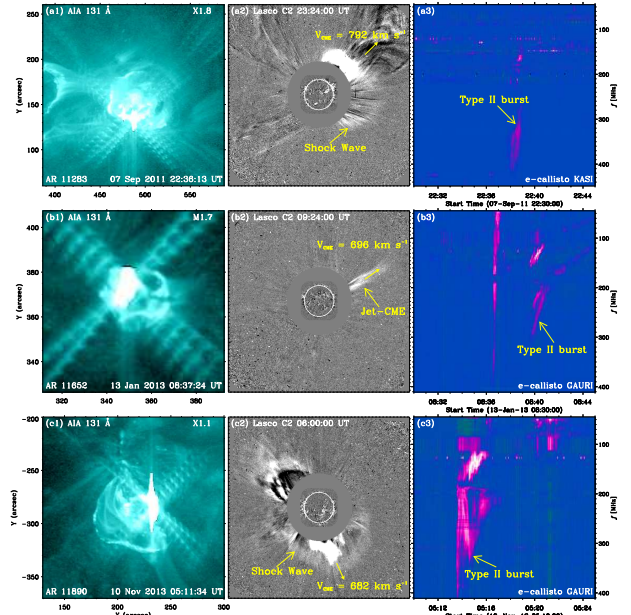


Figure 22. Left panels: Three CFs observed by AIA in 131 Å. Middle panels: Associated CMEs and shock waves observed by LASCO/C2. The apparent speeds of the CMEs are labeled. Right panels: Radio dynamic spectra of the three events recorded by the e-Callisto stations, showing the corresponding type II radio bursts with drifting frequency.

relatively lower intensities are pointed by the arrows. The right panels show radio dynamic spectra recorded by the e-Callisto stations, where type II radio bursts with drifting frequency are pointed by the arrows.

4. CONCLUSION AND DISCUSSION

In this paper, we conducted a comprehensive statistical analysis of 134 CFs observed by SDO/AIA from 2011

September to 2017 June, including four B-class, 82 C-class, 40 M-class, and eight X-class flares, respectively. The physical properties of CFs are derived, including the location, area (A_{CF}), equivalent radius (r_{CF}) assuming a semi-spherical fan dome, lifetime (τ_{CF}), and peak SXR flux in 1–8 Å. Combining with the observations from the SOHO/LASCO, WIND/WAVES, and radio stations of the e-Callisto network, we also explored the relations with remote brightenings, type III radio bursts, coronal jets, mini-filament eruptions, and CMEs. The main results are as follows:

1. All CFs are located in active regions, with the latitudes between -30° and 30° . Most of the areas are ≤ 5000 Mm^2 , with a mean value of ~ 1215 Mm^2 . The distribution could be fitted with a log-normal function, where $\mu = 6.51$, and $\sigma = 0.66$. The equivalent radii, representing the heights of magnetic null points, are between 6 and 87 Mm, with a mean value of ~ 16.8 Mm.
2. The lifetimes are between 4 and 205 minutes with a mean value of ~ 50 minutes. The distribution could also be fitted with a log-normal function, where $\mu = 3.6$, and $\sigma = 0.64$. There is a positive correlation between the lifetime and area, indicating that CFs with larger sizes tend to have longer lifetimes. The peak SXR flux in 1–8 Å is well in accord with a power-law distribution with an index of -1.42 .
3. For the 134 CFs, 57% of them are accompanied by remote brightenings or ribbons. The association rates with RBs increase with flare magnitudes. The mean values of total length (L_{RB}) and average distance (D_{RB}) of remote brightenings are ~ 84 Mm and ~ 89 Mm, respectively. A positive correlation exists between the two parameters, i.e., $D_{RB} = 67.56 + 0.26L_{RB}$.
4. About 47% and 51% of the 134 CFs are related to type III radio bursts and jets, respectively. The association rates are independent of flare classes, meaning that the production rates of type III radio bursts and jets depend mainly on the magnetic configuration instead of the flare energy. About 38% of CFs are related to mini-filament eruptions, and the association rates increase with flare classes.
5. Only 28% of CFs are related to CMEs, meaning that a majority of them are confined rather than eruptive events. This is in agreement with the relatively high association with remote brightenings considering the particular magnetic topology of CFs. The association rates with CMEs increase with flare magnitudes. The apparent speeds of CMEs are between 120 and 1203 km s^{-1} , with a mean value of ~ 517 km s^{-1} . There is a positive correlation between the CME speed and

peak SXR flux in 1–8 Å. The angular widths of CMEs (W_{CME}) are between 13° and 360° . A linear correlation exists between the angular width and apparent speed, indicating that faster CMEs tend to be wider.

Li et al. (2021) analyzed 719 flares during 2010–2019, finding that the total unsigned magnetic flux (Φ_{AR}) plays a decisive role in determining the eruptive character of a flare. For the 134 CFs, only 37 events are eruptive. The mean and median values of total area for the eruptive CFs are significantly greater than confined CFs. Hence, it is worthwhile investigating the total magnetic fluxes of CFs and justifying the conclusion of Li et al. (2021).

Of course, the current statistical work has limitations. Firstly, the sample is not large enough, leading to uncertainties in the results. Those flares with irregular or complex ribbons are excluded to minimize the ambiguity. The 134 flares were observed by SDO/AIA from 2011 September to 2017 June, including four B-class and eight X-class flares. The numbers of CFs will certainly grow after extending the dates to 2021 June for instance. Secondly, the shapes of outer ribbons are fitted with circles or ellipses, which is suitable in most cases. However, the fitting is unsatisfactory for irregular ribbons (Joshi et al. 2015). The method in Song & Tian (2018) seems to be more appropriate. Besides, the assumption of semi-spherical fan surface is not always valid to estimate the heights of null points (Vemareddy & Wiegmann 2014). Thirdly, the values of apparent speeds and angular widths of CMEs suffer from projection effect from a single viewpoint. Three-dimensional reconstruction of the shapes of CMEs is helpful to minimize this effect (Zhang 2022). Finally, the properties of CFs are still incomplete. The distribution of thermal energy and association rate with QPPs will be the focus of our next paper. The results are important to get a better understanding of solar flares and provide valuable constraints on 3D MHD simulations. In the future, new insights into CFs and the related activities will be obtained from observations of the Spectrometer/Telescope for Imaging X-rays (STIX; Krucker et al. 2020) on board Solar Orbiter (Müller et al. 2020).

The authors appreciate the referee for valuable suggestions and comments. The e-Callisto data are courtesy of the Institute for Data Science FHNW Brugg/Windisch, Switzerland. SDO is a mission of NASA's Living With a Star Program. AIA and HMI data are courtesy of the NASA/SDO science teams. This work is supported by the NSFC grants (No. 11790302, 11790300), and the Strategic Priority Research Program on Space Science, CAS (XDA15052200, XDA15320301).

REFERENCES

- Aulanier, G., Golub, L., DeLuca, E. E., et al. 2007, *Science*, 318, 1588. doi:10.1126/science.1146143
- Aulanier, G., Janvier, M., & Schmieder, B. 2012, *A&A*, 543, A110. doi:10.1051/0004-6361/201219311
- Benz, A. O., Grigis, P. C., Csillaghy, A., et al. 2005, *SoPh*, 226, 121. doi:10.1007/s11207-005-5254-5
- Bougeret, J.-L., Kaiser, M. L., Kellogg, P. J., et al. 1995, *SSRv*, 71, 231. doi:10.1007/BF00751331
- Brueckner, G. E., Howard, R. A., Koomen, M. J., et al. 1995, *SoPh*, 162, 357. doi:10.1007/BF00733434
- Cai, Z. M., Zhang, Q. M., Ning, Z. J., et al. 2021, *SoPh*, 296, 61. doi:10.1007/s11207-021-01805-5
- Cargill, P. J. 1994, *ApJ*, 422, 381. doi:10.1086/173733
- Carmichael, H. 1964, *NASA Special Publication*, 451
- Carrington, R. C. 1859, *MNRAS*, 20, 13. doi:10.1093/mnras/20.1.13
- Chae, J., Qiu, J., Wang, H., et al. 1999, *ApJL*, 513, L75. doi:10.1086/311910
- Chen, X., Yan, Y., Tan, B., et al. 2019, *ApJ*, 878, 78. doi:10.3847/1538-4357/ab1d64
- Christe, S., Hannah, I. G., Krucker, S., et al. 2008, *ApJ*, 677, 1385. doi:10.1086/529011
- Crosby, N. B., Aschwanden, M. J., & Dennis, B. R. 1993, *SoPh*, 143, 275. doi:10.1007/BF00646488
- Dai, J., Zhang, Q. M., Su, Y. N., et al. 2021, *A&A*, 646, A12. doi:10.1051/0004-6361/202039013
- Demoulin, P., Henoux, J. C., Priest, E. R., et al. 1996, *A&A*, 308, 643
- Dennis, B. R. 1985, *SoPh*, 100, 465. doi:10.1007/BF00158441
- De Pontieu, B., Title, A. M., Lemen, J. R., et al. 2014, *SoPh*, 289, 2733. doi:10.1007/s11207-014-0485-y
- Devi, P., Joshi, B., Chandra, R., et al. 2020, *SoPh*, 295, 75. doi:10.1007/s11207-020-01642-y
- Duan, Y., Shen, Y., Zhou, X., et al. 2022, *ApJL*, 926, L39. doi:10.3847/2041-8213/ac4df2
- Fletcher, L., Dennis, B. R., Hudson, H. S., et al. 2011, *SSRv*, 159, 19. doi:10.1007/s11214-010-9701-8
- Glesener, L., Krucker, S., & Lin, R. P. 2012, *ApJ*, 754, 9. doi:10.1088/0004-637X/754/1/9
- Hannah, I. G., Christe, S., Krucker, S., et al. 2008, *ApJ*, 677, 704. doi:10.1086/529012
- Hao, Q., Yang, K., Cheng, X., et al. 2017, *Nature Communications*, 8, 2202. doi:10.1038/s41467-017-02343-0
- Hernandez-Perez, A., Thalmann, J. K., Veronig, A. M., et al. 2017, *ApJ*, 847, 124. doi:10.3847/1538-4357/aa8814
- Hirayama, T. 1974, *SoPh*, 34, 323. doi:10.1007/BF00153671
- Hou, Y., Li, T., Yang, S., et al. 2019, *ApJ*, 871, 4. doi:10.3847/1538-4357/aaf4f4
- Janvier, M., Aulanier, G.,ariat, E., et al. 2013, *A&A*, 555, A77. doi:10.1051/0004-6361/201321164
- Ji, H., Huang, G., Wang, H., et al. 2006, *ApJL*, 636, L173. doi:10.1086/500203
- Jiang, C., Feng, X., Wu, S. T., et al. 2013, *ApJL*, 771, L30. doi:10.1088/2041-8205/771/2/L30
- Jing, J., Xu, Y., Cao, W., et al. 2016, *Scientific Reports*, 6, 24319. doi:10.1038/srep24319
- Joshi, N. C., Liu, C., Sun, X., et al. 2015, *ApJ*, 812, 50. doi:10.1088/0004-637X/812/1/50
- Joshi, N. C., Sterling, A. C., Moore, R. L., et al. 2017, *ApJ*, 845, 26. doi:10.3847/1538-4357/aa7c1b
- Joshi, N. C., Nishizuka, N., Filippov, B., et al. 2018, *MNRAS*, 476, 1286. doi:10.1093/mnras/sty322
- Joshi, N. C., Joshi, B., & Mitra, P. K. 2021, *MNRAS*, 501, 4703. doi:10.1093/mnras/staa3480
- Kashapova, L. K., Kupriyanova, E. G., Xu, Z., et al. 2020, *A&A*, 642, A195. doi:10.1051/0004-6361/201833947
- Kopp, R. A. & Pneuman, G. W. 1976, *SoPh*, 50, 85. doi:10.1007/BF00206193
- Krucker, S., Kontar, E. P., Christe, S., et al. 2011, *ApJ*, 742, 82. doi:10.1088/0004-637X/742/2/82
- Krucker, S., Hurford, G. J., Grimm, O., et al. 2020, *A&A*, 642, A15. doi:10.1051/0004-6361/201937362
- Kumar, P., Nakariakov, V. M., & Cho, K.-S. 2015, *ApJ*, 804, 4. doi:10.1088/0004-637X/804/1/4
- Kumar, P., Nakariakov, V. M., & Cho, K.-S. 2016, *ApJ*, 822, 7. doi:10.3847/0004-637X/822/1/7
- Kumar, P., Karpen, J. T., Antiochos, S. K., et al. 2021, *ApJ*, 907, 41. doi:10.3847/1538-4357/abca8b
- Lee, J., Karpen, J. T., Liu, C., et al. 2020, *ApJ*, 893, 158. doi:10.3847/1538-4357/ab80c4
- Lee, J., White, S. M., Chen, X., et al. 2020, *ApJL*, 901, L10. doi:10.3847/2041-8213/abb4dd
- Lemen, J. R., Title, A. M., Akin, D. J., et al. 2012, *SoPh*, 275, 17. doi:10.1007/s11207-011-9776-8
- Li, D., Ning, Z. J., & Zhang, Q. M. 2015, *ApJ*, 807, 72. doi:10.1088/0004-637X/807/1/72
- Li, H., Jiang, Y., Yang, J., et al. 2017, *ApJ*, 836, 235. doi:10.3847/1538-4357/aa5eac
- Li, T., Yang, S., Zhang, Q., et al. 2018, *ApJ*, 859, 122. doi:10.3847/1538-4357/aabe84
- Li, H. & Yang, J. 2019, *ApJ*, 872, 87. doi:10.3847/1538-4357/aafb3a
- Li, D., Feng, S., Su, W., et al. 2020, *A&A*, 639, L5. doi:10.1051/0004-6361/202038398
- Li, T., Chen, A., Hou, Y., et al. 2021, *ApJL*, 917, L29. doi:10.3847/2041-8213/ac1a15

- Liu, C., Deng, N., Lee, J., et al. 2013, *ApJL*, 778, L36.
doi:10.1088/2041-8205/778/2/L36
- Liu, C., Deng, N., Liu, R., et al. 2015, *ApJL*, 812, L19.
doi:10.1088/2041-8205/812/2/L19
- Liu, C., Lee, J., & Wang, H. 2019, *ApJ*, 883, 47.
doi:10.3847/1538-4357/ab3923
- Liu, C., Prasad, A., Lee, J., et al. 2020, *ApJ*, 899, 34.
doi:10.3847/1538-4357/ab9cbe
- Lu, E. T. & Hamilton, R. J. 1991, *ApJL*, 380, L89.
doi:10.1086/186180
- Lu, L., Feng, L., Li, D., et al. 2021, *ApJS*, 253, 29.
doi:10.3847/1538-4365/abd79b
- Mancuso, S., Frassati, F., Bemporad, A., et al. 2019, *A&A*, 624, L2. doi:10.1051/0004-6361/201935157
- Masson, S., Pariat, E., Aulanier, G., et al. 2009, *ApJ*, 700, 559.
doi:10.1088/0004-637X/700/1/559
- Masson, S., Pariat, É., Valori, G., et al. 2017, *A&A*, 604, A76.
doi:10.1051/0004-6361/201629654
- Mitra, P. K. & Joshi, B. 2021, *MNRAS*, 503, 1017.
doi:10.1093/mnras/stab175
- Morosan, D. E., Gallagher, P. T., Zucca, P., et al. 2014, *A&A*, 568, A67. doi:10.1051/0004-6361/201423936
- Müller, D., St. Cyr, O. C., Zouganelis, I., et al. 2020, *A&A*, 642, A1. doi:10.1051/0004-6361/202038467
- Ning, Z., Wang, Y., Hong, Z., et al. 2022, *SoPh*, 297, 2.
doi:10.1007/s11207-021-01935-w
- Ontiveros, V. & Vourlidas, A. 2009, *ApJ*, 693, 267.
doi:10.1088/0004-637X/693/1/267
- Pariat, E., Antiochos, S. K., & DeVore, C. R. 2009, *ApJ*, 691, 61.
doi:10.1088/0004-637X/691/1/61
- Pariat, E., Antiochos, S. K., & DeVore, C. R. 2010, *ApJ*, 714, 1762. doi:10.1088/0004-637X/714/2/1762
- Pesnell, W. D., Thompson, B. J., & Chamberlin, P. C. 2012, *SoPh*, 275, 3. doi:10.1007/s11207-011-9841-3
- Pontin, D. I., Bhattacharjee, A., & Galsgaard, K. 2007, *Physics of Plasmas*, 14, 052106. doi:10.1063/1.2722300
- Pontin, D. I., Priest, E. R., & Galsgaard, K. 2013, *ApJ*, 774, 154.
doi:10.1088/0004-637X/774/2/154
- Priest, E. R. & Pontin, D. I. 2009, *Physics of Plasmas*, 16, 122101.
doi:10.1063/1.3257901
- Qiu, J., Lee, J., Gary, D. E., et al. 2002, *ApJ*, 565, 1335.
doi:10.1086/324706
- Qiu, J., Longcope, D. W., Cassak, P. A., et al. 2017, *ApJ*, 838, 17.
doi:10.3847/1538-4357/aa6341
- Reid, H. A. S. & Ratcliffe, H. 2014, *Research in Astronomy and Astrophysics*, 14, 773. doi:10.1088/1674-4527/14/7/003
- Reid, H. A. S., Vilmer, N., Aulanier, G., et al. 2012, *A&A*, 547, A52. doi:10.1051/0004-6361/201219562
- Savcheva, A., Pariat, E., McKillop, S., et al. 2016, *ApJ*, 817, 43.
doi:10.3847/0004-637X/817/1/43
- Scherrer, P. H., Schou, J., Bush, R. I., et al. 2012, *SoPh*, 275, 207.
doi:10.1007/s11207-011-9834-2
- Shen, Y., Qu, Z., Zhou, C., et al. 2019, *ApJL*, 885, L11.
doi:10.3847/2041-8213/ab4cf3
- Shibata, K. & Magara, T. 2011, *Living Reviews in Solar Physics*, 8, 6. doi:10.12942/lrsp-2011-6
- Shibata, K., Nakamura, T., Matsumoto, T., et al. 2007, *Science*, 318, 1591. doi:10.1126/science.1146708
- Song, Y. & Tian, H. 2018, *ApJ*, 867, 159.
doi:10.3847/1538-4357/aae5d1
- Song, Y. L., Guo, Y., Tian, H., et al. 2018, *ApJ*, 854, 64.
doi:10.3847/1538-4357/aaa7f1
- Sturrock, P. A. 1966, *Nature*, 211, 695. doi:10.1038/211695a0
- Sun, X., Hoeksema, J. T., Liu, Y., et al. 2013, *ApJ*, 778, 139.
doi:10.1088/0004-637X/778/2/139
- Temmer, M., Veronig, A., Hanslmeier, A., et al. 2001, *A&A*, 375, 1049. doi:10.1051/0004-6361:20010908
- Vemareddy, P. & Wiegmann, T. 2014, *ApJ*, 792, 40.
doi:10.1088/0004-637X/792/1/40
- Veronig, A., Temmer, M., Hanslmeier, A., et al. 2002, *A&A*, 382, 1070. doi:10.1051/0004-6361:20011694
- Vourlidas, A., Lynch, B. J., Howard, R. A., et al. 2013, *SoPh*, 284, 179. doi:10.1007/s11207-012-0084-8
- Wang, H. & Liu, C. 2012, *ApJ*, 760, 101.
doi:10.1088/0004-637X/760/2/101
- Wyper, P. F. & DeVore, C. R. 2016, *ApJ*, 820, 77.
doi:10.3847/0004-637X/820/1/77
- Wyper, P. F., DeVore, C. R., Karpen, J. T., et al. 2016, *ApJ*, 827, 4.
doi:10.3847/0004-637X/827/1/4
- Wyper, P. F., Antiochos, S. K., & DeVore, C. R. 2017, *Nature*, 544, 452. doi:10.1038/nature22050
- Xu, Z., Yang, K., Guo, Y., et al. 2017, *ApJ*, 851, 30.
doi:10.3847/1538-4357/aa9995
- Yang, K., Guo, Y., & Ding, M. D. 2015, *ApJ*, 806, 171.
doi:10.1088/0004-637X/806/2/171
- Yang, S. & Zhang, J. 2018, *ApJL*, 860, L25.
doi:10.3847/2041-8213/aacaf9
- Yang, J., Hong, J., Li, H., et al. 2020, *ApJ*, 900, 158.
doi:10.3847/1538-4357/aba7c0
- Yang, S., Zhang, Q., Xu, Z., et al. 2020, *ApJ*, 898, 101.
doi:10.3847/1538-4357/ab9ac7
- Yashiro, S., Gopalswamy, N., Michalek, G., et al. 2004, *Journal of Geophysical Research (Space Physics)*, 109, A07105.
doi:10.1029/2003JA010282
- Yashiro, S., Gopalswamy, N., Akiyama, S., et al. 2005, *Journal of Geophysical Research (Space Physics)*, 110, A12S05.
doi:10.1029/2005JA011151
- Yashiro, S., Akiyama, S., Gopalswamy, N., et al. 2006, *ApJL*, 650, L143. doi:10.1086/508876

- Yashiro, S., Michalek, G., & Gopalswamy, N. 2008, *Annales Geophysicae*, 26, 3103. doi:10.5194/angeo-26-3103-2008
- Zhang, Q. M. 2020, *A&A*, 642, A159. doi:10.1051/0004-6361/202038557
- Zhang, Q. M. 2022, arXiv:2202.10676
- Zhang, Q. M. & Ni, L. 2019, *ApJ*, 870, 113. doi:10.3847/1538-4357/aaf391
- Zhang, Q.-M., Guo, Y., Chen, P.-F., et al. 2010, *Research in Astronomy and Astrophysics*, 10, 461. doi:10.1088/1674-4527/10/5/006
- Zhang, Q. M., Ning, Z. J., Guo, Y., et al. 2015, *ApJ*, 805, 4. doi:10.1088/0004-637X/805/1/4
- Zhang, Q. M., Li, D., Ning, Z. J., et al. 2016a, *ApJ*, 827, 27. doi:10.3847/0004-637X/827/1/27
- Zhang, Q. M., Li, D., & Ning, Z. J. 2016b, *ApJ*, 832, 65. doi:10.3847/0004-637X/832/1/65
- Zhang, Q. M., Li, D., & Huang, Y. 2019a, *ApJ*, 870, 109. doi:10.3847/1538-4357/aaf4b7
- Zhang, Q. M., Cheng, J. X., Feng, L., et al. 2019b, *ApJ*, 883, 124. doi:10.3847/1538-4357/ab3a52
- Zhang, Q. M., Yang, S. H., Li, T., et al. 2020, *A&A*, 636, L11. doi:10.1051/0004-6361/202038072
- Zhang, Q. M., Huang, Z. H., Hou, Y. J., et al. 2021, *A&A*, 647, A113. doi:10.1051/0004-6361/202038924
- Zimovets, I. V., McLaughlin, J. A., Srivastava, A. K., et al. 2021, *SSRv*, 217, 66. doi:10.1007/s11214-021-00840-9
- Zucca, P., Morosan, D. E., Rouillard, A. P., et al. 2018, *A&A*, 615, A89. doi:10.1051/0004-6361/201732308